RESEARCH ARTICLE

Omnidirectional Circularly Polarized Monopole Antennas on Artificial Magnetic Conductor Ground Plane

PISIT JANPANGNGERN[1], **RYUJI KUSE**[2], **(Member, IEEE),**
CHUWONG PHONGCHAROENPANICH[1], **(Member, IEEE),**
AND TAKESHI FUKUSAKO[2], **(Senior Member, IEEE)**

[1]School of Engineering, King Mongkut's Institute of Technology Ladkrabang, Bangkok 10520, Thailand
[2]Faculty of Advanced Science and Technology, Kumamoto University, Kumamoto 860-8555, Japan

Corresponding author: Chuwong Phongcharoenpanich (chuwong.ph@kmitl.ac.th)

ABSTRACT This research proposes omnidirectional circularly polarized monopole antennas (OCPA) with single-annular (SA-AMC) and dual-annular artificial magnetic conductor (DA-AMC) ground planes. The aim of the proposed antenna scheme is to circumvent the design rigidity of conventional OCPA whose inherent shortcoming is fixed bottom ground plane size. The OCPA with SA-AMC ground plane consists of a monopole element, four diagonally adjoined parasitic elements to convert linear to circular polarizations, and an SA-AMC ground plane. The OCPA with DA-AMC ground plane consists of a monopole element, four diagonally adjoined parasitic elements, and a DA-AMC ground plane. Unlike the conventional OCPA, the bottom ground plane radius (R_g) of the OCPA with SA- and DA-AMC ground planes can be varied between $18.4 - 188.4$ mm; and $29.2 - 119.2$ mm, respectively, without affecting the omnidirectionality and impedance and axial ratio (AR) bandwidths of the OCPA. Furthermore, the SA- and DA-AMC ground planes effectively improve the impedance ($|S_{11}| \leq -10$ dB) and AR bandwidths (AR ≤ 3 dB) while reducing leakage current on the coaxial feeder cable. The measured $|S_{11}|$ and AR bandwidths of the OCPA with SA-AMC ground plane, given the optimal R_g of 18.4 mm, are 8.08% ($5.34 - 5.79$ GHz) and 4.38% ($5.36 - 5.60$ GHz), while those of the OCPA with DA-AMC ground plane, given the optimal R_g of 29.2 mm, are 14.37% ($5.10 - 5.89$ GHz) and 19.85% ($4.90 - 5.98$ GHz). The novelty of this research lies in the use of SA- and DA-AMC structures to circumvent the design rigidity of the conventional OCPA. Essentially, the integration of the AMC structures offers design flexibility in the realization of OCPA.

INDEX TERMS Artificial magnetic conductor, circular polarization, monopole antenna, omnidirectional pattern.

I. INTRODUCTION

Unlike linearly polarized antennas, circularly polarized (CP) antennas contribute to reducing the effects of multipath fading and polarization mismatch loss in the radio link. As a result, CP antennas are widely used in wireless communication devices. Modern wireless communication devices

The associate editor coordinating the review of this manuscript and approving it for publication was Debabrata K. Karmokar.

require CP antennas with omnidirectionality for a variety of applications, such as wireless local area network (WLAN), sensor network, mobile satellite, and 5G mobile technology. A large number of studies have focused on omnidirectional circularly polarized antennas (OCPAs) [1], [2], [3], [4], [5], [6], [7], [8], [9], [10], [11], [12], [13], [14], [15], [16], [17], [18], [19], [20], [21], [22], [23].

A typical OCPA consists of horizontal radiating elements on the ground plane and vertical elements [1], [4], [5], [6],

[7], [8], [9], [10], [11], [12], [14], [15], [16], [17], [18], [19], [20]. The phase difference between the electric current of the horizontal elements (i.e., horizontal component) and the vertical elements (vertical component) must be 90° to generate circular polarization. Previous studies demonstrated that the ground plane size or radius largely affects the horizontal component of circular polarization [1], [4], [5], [6], [7], [8], [9], [10], [11], [12], [14], [15], [16], [17], [18], [19], [20]. Specifically, in [2], [3], [13], [21], [22], and [23], OCPAs with polarizer-like parasitic elements were proposed to convert linear polarization (LP) to circular polarization. However, the existing research studies attach little emphasis to the effect of variable ground plane sizes or radii on the impedance and axial ratio bandwidths, radiation pattern, and leakage current.

The ground plane size plays an important role in the design and performance of OCPA [1], [3], [15]. Excessive OCPA ground plane sizes result in non-circular polarization or non-omnidirectional CP radiation. Meanwhile, if the ground plane size is too small, an external balun is required to reduce leakage current on the coaxial cable and achieve omnidirectionality [11], [14], [15].

To the best of the authors' knowledge, very limited attempts have been made to address the shortcomings of the conventional OCPAs. In [16], a low-profile wideband CP circular patch antenna with two monopolar modes connected to a modified ground plane by conductive vias could achieve omnidirectional CP but failed to reduce the leakage current on the coaxial cable. In [17], a patch antenna with vortex slots and shorting vias could achieve omnidirectional CP but narrow impedance and AR bandwidths.

In this research, two artificial magnetic conductor (AMC) structures are utilized to circumvent the design rigidity of the ground plane size while improving the impedance and AR bandwidths and reducing the leakage current. The proposed AMC structures include the single-annular (SA-AMC) and dual-annular AMC (DA-AMC) structures, which are used as the OCPA ground plane. The SA-AMC ground plane has an annular containing eight circularly arrayed fan-shaped unit cells without vias, and the DA-AMC ground plane has two annuli (inner and outer annuli). The inner and outer annuli of the DA-AMC contain eight and fifteen circularly arrayed fan-shaped unit cells without vias. The AMC technology has been used in antenna development to achieve bandwidth enhancement, low-profile design, and radiation improvement [24], [25], [26], [27], [28], [29], [30], [31]. Unlike in [31] whose similar annular AMC structure requires vias, the proposed SA- and DA-AMC ground planes are realized without vias.

Specifically, this research proposes omnidirectional circularly polarized monopole antennas with SA-AMC and DA-AMC ground planes for Internet of Things (IoT) applications, such as intelligent transport systems and vehicle-to-vehicle communication. The SA- and DA-AMC ground planes improve the impedance ($|S_{11}| \leq -10$ dB) and AR bandwidths (AR ≤ 3 dB) of the OCPA while reducing the leakage current on the bottom ground plane and
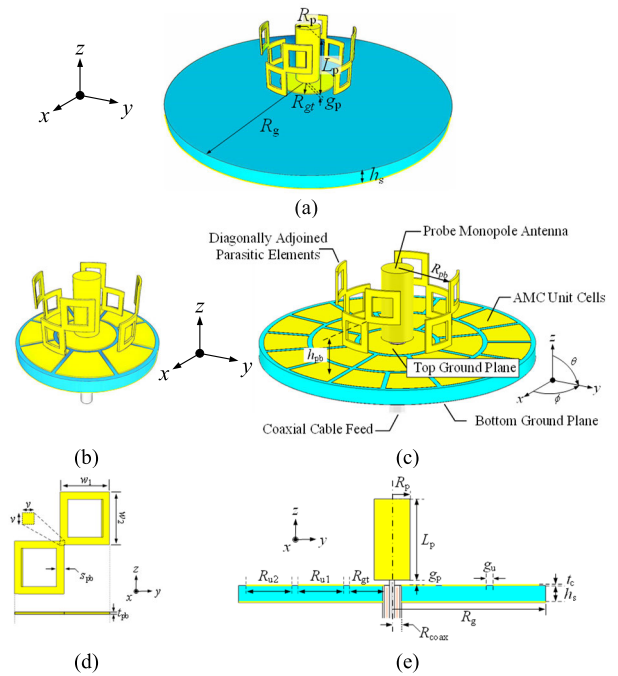
FIGURE 1. Geometry of the omnidirectional circularly polarized monopole antennas under study: (a) Structure A, (b) Structure B, (c) Structure C, (d) diagonally-adjoined parasitic element, (e) cross-sectional view of Structure C.

coaxial feeder cable. The reduced leakage current could be attributed to high impedance on the surface of the SA- and DA-AMC structures. Unlike the conventional OCPA which suffers the design rigidity (i.e., the fixed ground plane size; 39.2 mm), the integration of SA-AMC or DA-AMC ground plane with the OCPA affords the antenna developers with design flexibility (i.e., the adjustable AMC ground plane sizes; 18.4 – 188.4 mm for the SA-AMC ground plane; and 29.2 – 119.2 mm for the DA-AMC ground plane).

Moreover, in this research, the OCPAs with SA- and DA-AMC ground plane are experimented with an aluminum installation base of different radii (119.2 and 188.4 mm) to investigate the effect of the installation base on the omnidirectionality of OCPA, given the bottom ground plane radius (R_g) of 18.4 mm and 29.2 mm for the SA- and DA-AMC structures, respectively.

The organization of this paper is as follows: Section I is the introduction. Section II details the antenna configuration. Section III describes the characteristics of OCPAs with conventional ground plane, and Section IV deals with the characteristics of OCPA with AMC ground planes. Section V discusses the effect of the AMC on CP waves and leakage current. The concluding remarks are provided in Section VI.

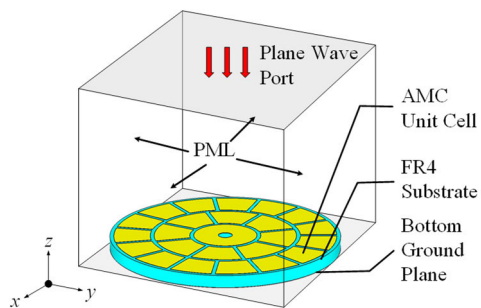## II. ANTENNA CONFIGURATION AND EFFECTS ON LEAKAGE CURRENT

Fig. 1(a) shows the conventional OCPA (i.e., Structure A). Figs. 1(b) and (c) show the proposed OCPAs with SA-AMC (Structure B) and DA-AMC ground plane

TABLE 1. Optimal dimensions of structure B (Unit: mm).

L_p	R_p	g_p	w_1	w_2	s_{pb}
16.20	3.90	1.00	7.20	7.20	1.00
$0.297\,\lambda_c$	$0.071\,\lambda_c$	$0.018\,\lambda_c$	$0.132\,\lambda_c$	$0.132\,\lambda_c$	$0.018\,\lambda_c$
v	R_{pb}	h_{pb}	t_{pb}	R_{u1}	R_{gt}
0.50	11.50	11.50	0.5	9.00	7.40
$0.0092\,\lambda_c$	$0.211\,\lambda_c$	$0.211\,\lambda_c$	$0.0092\,\lambda_c$	$0.165\,\lambda_c$	$0.135\,\lambda_c$
g_u	R_g	h_s	t_c	R_{coax}	
1.00	18.40	3.20	0.018	1.80	
$0.018\,\lambda_c$	$0.337\,\lambda_c$	$0.058\,\lambda_c$	$0.0003\lambda_c$	$0.033\,\lambda_c$	

TABLE 2. Optimal dimensions of structure C (Unit: mm).

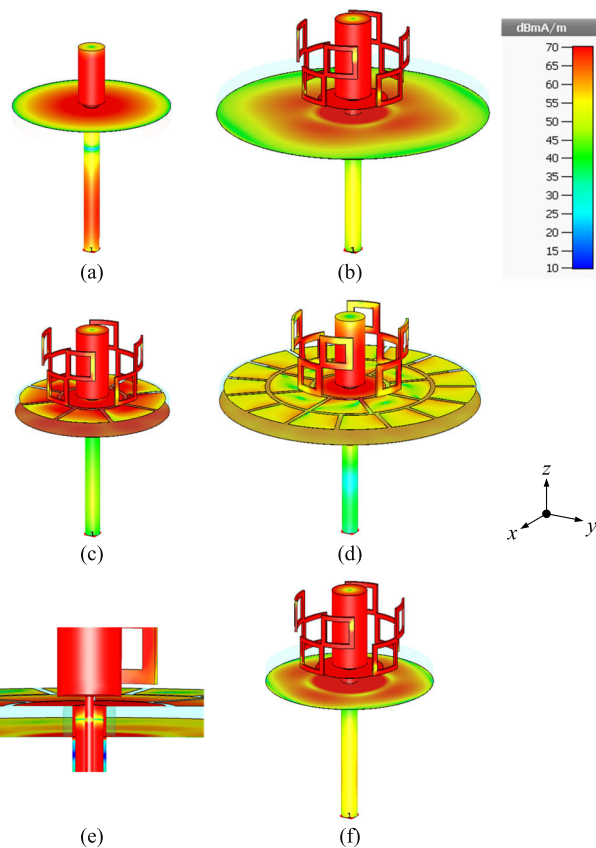| L_p	R_p	g_p	w_1	w_2	s_{pb}
15.5	3.4	1.00	7.40	7.40	1.50
$0.284\lambda_c$	$0.062\lambda_c$	$0.018\lambda_c$	$0.135\lambda_c$	$0.135\lambda_c$	$0.027\lambda_c$
v	R_{pb}	h_{pb}	t_{pb}	R_{u1}	R_{u2}
0.50	12.50	11.50	0.5	9.00	9.20
$0.0092\lambda_c$	$0.229\lambda_c$	$0.211\lambda_c$	$0.0092\lambda_c$	$0.165\lambda_c$	$0.168\lambda_c$
R_{gt}	g_u	R_g	h_s	t_c	R_{coax}
8.00	1.00	29.20	3.20	0.018	1.80
$0.146\lambda_c$	$0.018\lambda_c$	$0.535\lambda_c$	$0.058\lambda_c$	$0.0003\lambda_c$	$0.033\lambda_c$

FIGURE 2. Geometry of AMC model to simulate the reflection phase.

FIGURE 3. Surface current distribution given the top ground plane radius (R_p) of 3 mm at 5.5 GHz: (a) a typical monopole antenna with a ground plane radius (R_g) of 18 mm ($0.33\lambda_c$), (b) Structure A with $R_g = 29.2$ mm ($0.54\lambda_c$), (c) Structure B with $R_g = 18.4$ mm ($0.34\lambda_c$), (d) Structure C with $R_g = 29.2$ mm ($0.54\lambda_c$), (e) cross-sectional view of Structure C, (f) Structure A with $R_g = 18.4$ mm ($0.34\lambda_c$).

(Structure C). Figs. 1(d) and (e) illustrate the geometry of a diagonally-adjoined parasitic element and the cross-sectional view of Structure C, respectively.

The structural parameters of Structure A are as follows: $L_p = 16.9$ mm, $R_p = 3.9$ mm, $R_{gt} = 7.4$ mm, $R_g = 39.2$ mm, $g_p = 1$ mm, $h_s = 3.2$ mm, $w_1 = w_2 = 7.2$ mm, $v = 0.5$ mm, $h_{pb} = 11.5$ mm, and $s_{pb} = 1.0$ mm. The top ground plane (R_{gt}) of Structure A sits on a substrate (turquoise color) and a large bottom ground plane (R_g) of perfect electric conductor (PEC) underneath the substrate, as shown in Fig. 1(a). In addition, four diagonally adjoined parasitic elements to convert LP to CP encircle the monopole element.

Structure B consists of a monopole element with a radius of R_p, four diagonally adjoined parasitic elements suspended over the top ground plane (with a radius of R_{gt}) at a height of h_{pb} to covert linear to circular polarization, and an SA-AMC ground plane. Structure C consists of a monopole element, four diagonally adjoined parasitic elements, and a DA-AMC ground plane. Tables 1 and 2 tabulate the optimal dimensions of Structures B and C, where λ_c is the free-space wavelength at 5.5 GHz.

The SA-AMC ground plane has one annular containing 8 circularly arrayed fan-shaped unit cells with equal spacing (g_u), and the DA-AMC ground plane has two annuli (inner and outer annuli). The inner and outer annuli of the DA-AMC contain 8 and 15 circularly arrayed fan-shaped unit cells with equal spacing (g_u), respectively. The AMC fan-shaped unit cells are $18\mu m$ in thickness, arrayed on top of the substrate with a radius (R_g) of 18.4 mm (for Structure B) and 29.2 mm (for Structure C). The dielectric substrate (turquoise color) is of Chukoh CGP-500A substrate ($\varepsilon_r = 2.6$ and $\tan\delta = 0.0025$). The top ground plane is connected to the bottom ground plane by the coaxial feeder cable through a through-hole.

Fig. 2 shows the geometry of the AMC model (i.e., Structure C) to simulate the reflection phase. In the design, the parameters of AMC ground plane are optimized using the analysis model technique. In [29], analysis modeling was used to optimize the parameters of the proposed circular high impedance surface (HIS). The simulation is carried out using CST Microwave Studio with perpendicular incident wave at $\theta = 0°$, and the entire AMC structure is enclosed in the absorbing boundaries of perfectly matched layer (PML). The

simulated reflection phase of 0° is achieved near the target frequency of 5.5 GHz.

Figs. 3(a)-(d) show the surface current distribution at 5.5 GHz of a typical monopole antenna, the conventional OCPA (Structure A), the OCPA with SA-AMC ground plane (Structure B), and the OCPA with DA-AMC ground plane (Structure C). Meanwhile, Figs. 3(e) and (f) show the surface current distribution between the top and bottom ground planes of Structure C; and the current distribution of Structure A given R_g = 18.4 mm (to compare with Structure B in Fig. 3(c)).

In Fig. 3(a), strong leakage current is visible on the coaxial feeder cable and the monopole radiator (given R_g = 18 mm ($0.33\lambda_c$)), resulting in impedance mismatch and non-omnidirectionality. In Fig. 3(b) (Structure A), given R_g = 29.2 mm ($0.54\lambda_c$), the leakage current on the coaxial feeder cable is substantially reduced, vis-à-vis the typical monopole antenna (Fig. 3(a)). The weaker leakage current is attributable to the larger ground plane of Structure A.

In Fig. 3(c) (Structure B), given R_g = 18.4 mm ($0.34\lambda_c$), the leakage current on the coaxial feeder cable of Structure B is further reduced, vis-à-vis the typical monopole antenna (Fig. 3(a)) and Structure A (Fig. 3(b)). Besides, strong current resonance is visible around the center of the SA-AMC ground plane. In Fig. 3(d) (Structure C), given R_g = 29.2 mm ($0.54\lambda_c$), the leakage current on the coaxial cable is significantly reduced. The current resonance is strong around the center of the DA-AMC ground plane. The significantly lower leakage current could be attributed to the double annuli of the AMC structure of Structure C.

Fig. 3(e) shows the surface current between the top and bottom ground planes of Structure C. The top ground plane is connected to the bottom ground plane by the coaxial feeder cable through a through-hole. The surface currents are concentrated around the center of the top and bottom ground planes as well as on the coaxial feeder cable.

In the SA- and DA-AMC ground planes, the through-hole at the center serves as inductance (L_g), the circularly arrayed fan-shaped unit cells as inductance (L_r, L_φ), the space between unit cells as capacitance (C_r, C_φ), and the space between unit cells and the bottom ground plane as capacitance (C_g), where the subscripts r and φ indicate the radial and circumferential components in the AMC. The current resonance on Structures B and C in the radial and circumferential directions are attributable to the parallel resonators of L_g, L_r and C_g; and L_φ, C_φ and C_g [32]. The lower leakage current is attributable to high impedance on the surface of Structures B and C.

III. CHARACTERISTICS OF OCPAS WITH CONVENTIONAL GROUND PLANES (STRUCTURE A)

Fig. 4(a) show the simulated impedance bandwidth ($|S_{11}| \leq -10$ dB) of Structure A under various R_g: 9.4, 39.2, 54.0, 75.0, and 100.0 mm. Given the target center frequency of 5.5 GHz, the bottom ground plane radius (R_g) ≥ 39.2 mm could achieve satisfactory impedance matching.
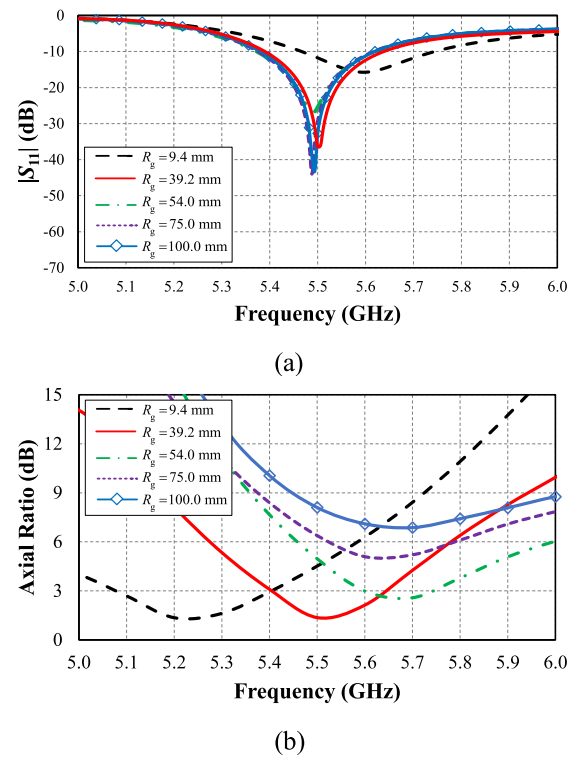

(a)

(b)

FIGURE 4. Simulated $|S_{11}|$ of Structure A under different bottom ground plane radii (R_g) and the corresponding AR given R_g = 9.4 mm at (θ, φ) = (90°, 0°) and R_g = 39.2 – 100.0 mm at (θ, φ) = (75°, 0°): a) $|S_{11}|$, b) AR.
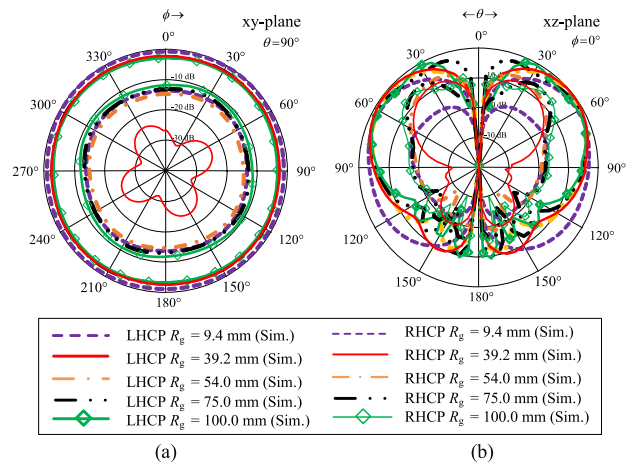

(a)   (b)

FIGURE 5. Simulated radiation patterns of Structure A under different bottom ground plane radii (R_g): (a) xy-, (b) xz-plane.

Fig. 4(b) also shows the simulated AR of Structure A under various R_g, given that the minimum AR are achieved at the elevation and azimuth angles (θ, ϕ) of 90°, 0° for R_g = 9.4 mm and at (θ, ϕ) = (75°, 0°) for R_g = 39.2 – 100.0 mm. The optimal R_g is 39.2 mm. As R_g becomes smaller (< 39.2 mm), the leakage current is generated on the coaxial feeder cable (as shown in Fig. 3(f)), resulting in higher AR. Meanwhile, as R_g becomes larger (> 39.2 mm), the cross-polarization levels (XPL) increase, resulting in AR deterioration. Essentially, the AR of Structure A (i.e., the
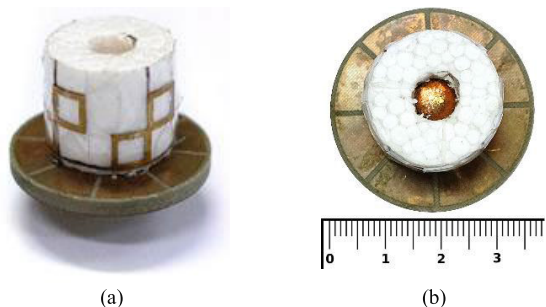
FIGURE 6. Prototype of Structure B: (a) Perspective view, (b) Top view.

FIGURE 7. Simulated reflection phase of SA-AMC for Structure B.

conventional OCPA) is sensitive to the bottom ground plane size or radius (R_g). As a result, the optimal R_g of Structure A is 39.2 mm ($0.72\lambda_c$), achieving the $|S_{11}|$ and 3-dB AR bandwidths of 4.49% (5.380 –5.638 GHz) and 4.68% (5.390 –5.638 GHz), respectively.

Figs. 5 (a)-(b) show the simulated xy- and xz-plane radiation patterns of Structure A under different R_g (9.4, 39.2, 54.0, 75.0, and 100.0 mm), given the target center frequency of 5.5 GHz. The xy- and xz-plane radiation patterns of Structure A are near-circular polarization, given that $R_g \leq 39.2$ mm. (Note: The radiation pattern is not circular polarization if $R_g > 39.2$ mm.) Given the optimal R_g of 39.2 mm, the xz-plane half power beamwidth (HPBW) is 56° and the xy- and xz-plane XPL, in relation to the left-hand circular polarization (LHCP), are both –12.7 dB. The maximum gain of Structure A antenna is 2.85 dBic. The larger ground plane ($R_g > 39.2$ mm) underneath the substrate of Structure A significantly tilts the elevation angle (θ) of the main beam direction upward from 90° to 75°.

In Structure A (i.e., the conventional OCPA), given $R_g \leq 39.2$ mm and 5.5 GHz, the XPL is < -15 dB, resulting in AR < 3 dB, but AR exceeds 3 dB if $R_g > 39.2$ mm. As R_g decreases ($R_g < 39.2$ mm), the leakage current is generated on the coaxial feeder cable, adversely affecting the impedance matching.

Since the optimal bottom ground plane radius (R_g) of Structure A must be 39.2 mm ($R_g = 39.2$ mm) to achieve the near-omnidirectional CP radiation pattern, the conventional OCPA (or Structure A) suffers from the design rigidity. In other words, antenna developers are limited to the fixed ground plane size (i.e., $R_g = 39.2$ mm). If $R_g < 39.2$ mm, the AR deviates from the target frequency; and if $R_g > 39.2$ mm, the radiation pattern shows high AR. To overcome the shortcoming of the conventional OCPA (Structure A), the subsequent section discusses the OCPA with SA- and DA-AMC ground planes.

IV. CHARACTERIZATION OF ANTENNAS WITH GROUND PLANES

A. OMNIDIRECTIONAL CIRCULARLY POLARIZED MONOPOLE ANTENNA WITH SA-AMC (STRUCTURE B)

As previously discussed, the bottom ground plane radius (R_g) affects the $|S_{11}|$ and AR bandwidths and radiation patterns of
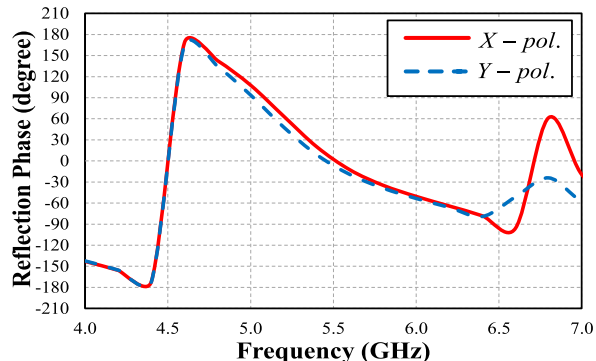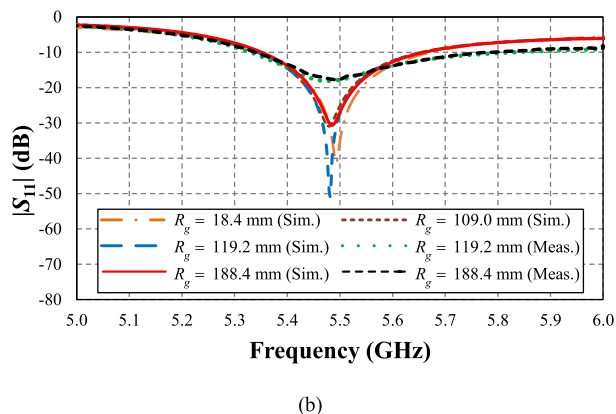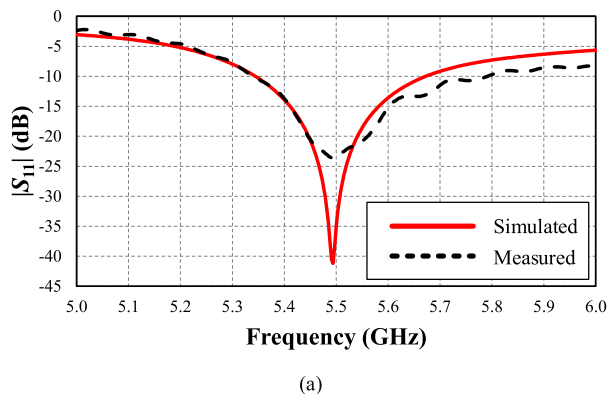

(a)

(b)

FIGURE 8. Simulated and measured $|S_{11}|$ of Structure B under variable bottom ground plane radii (R_g): (a) the optimal R_g of 18.4 mm, (b) variable R_g.

the conventional OCPA. To overcome the shortcomings of the conventional OCPA, SA-AMC with the unit-cell radius of R_{u1} is incorporated into the antenna structure. To verify the simulation results, a prototype of Structure B (i.e., the OCPA with SA-AMC ground plane) was fabricated, and experiments were subsequently carried out and results compared. Fig. 6 shows the prototype of Structure B based on the structural parameters in Table 1.

In the prototype, Styrofoam is used to prop up the diagonally adjoined parasitic elements. The dieletric constants of air ($\varepsilon_r = 1.00059$) and Styrofoam (1.1) are almost identical,
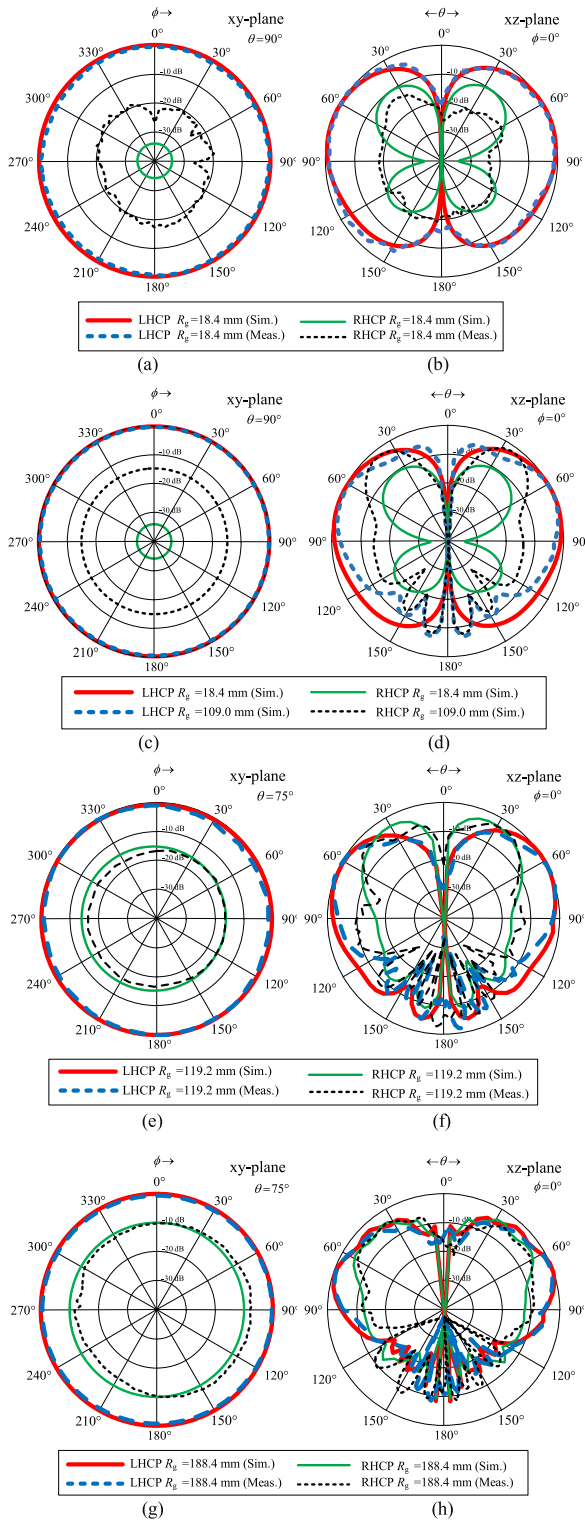
FIGURE 9. Simulated and measured radiation patterns of Structure B at 5.5 GHz: (a) *xy*-plane for R_g= 18.4 mm ($0.34\lambda_c$), (b) *xz*-plane for R_g = 18.4 mm ($0.34\lambda_c$), (c) *xy*-plane for R_g = 109.0 mm ($\cong 2\lambda_c$), (d) *xz*-plane for R_g = 109.0 mm ($\cong 2\lambda_c$), (e) *xy*-plane for R_g = 119.2 mm ($\cong 2.15\lambda_c$), (f) *xz*-plane for R_g = 119.2 mm ($\cong 2.15\lambda_c$), (g) *xy*-plane for R_g = 188.4 mm, (h) *xz*-plane for R_g = 188.4 mm ($\cong 3.50\lambda_c$).

resulting in a negligible effect on the antenna performance. The monopole element is constructed from a copper rod,

and the radius of the monopole element (R_p) primarily influences the impedance matching. Additionally, the length of the monopole element (L_p) significantly affects the resonance frequency.

In Fig. 7, at 5.5 GHz, the simulated reflection phase in both x- and y- polarizations of the SA-AMC ground plane (Structure B) approach zero, with the reflection phase bandwidth (AMC band) between $-90°$ (upper frequency limit) and $+90°$ (lower frequency limit), covering $5.1 - 6.5$ GHz (24.13%).

Fig. 8(a) shows the simulated and measured $|S_{11}|$ of Structure B, given the optimal $R_g = 18.4$ mm (Table 1). The simulated and measured minimum impedance matching of Structure B are -41.17 dB and -23.46 dB at 5.49 GHz. The simulated and measured results are agreeable.
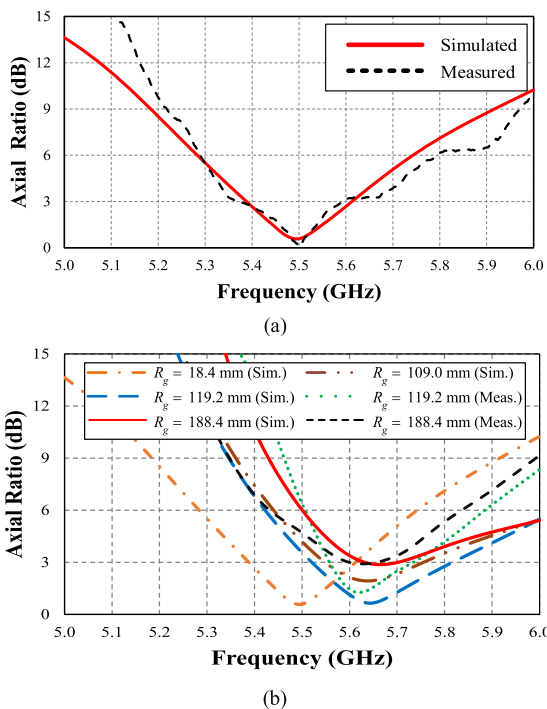
Fig. 8(b) shows the simulated and measured reflection coefficients ($|S_{11}| \leq -10$ dB) of Structure B under different R_g, whereby only the bottom ground plane (underneath the substrate) is enlarged while the SA-AMC (i.e., the number of unit cells and annular size) remains constant. The results indicate that the impedance bandwidth ($|S_{11}| \leq -10$ dB) of Structure B remains relatively constant at around 6.34%, covering $5.34 - 5.69$ GHz, despite the enlargement of R_g from 18.4 to 188.4 mm. For $R_g > 188.4$ mm, the simulated and measured impedance bandwidths ($|S_{11}| \leq -10$ dB) remain relatively unchanged. (Note: The simulated and measured $|S_{11}|$ for $R_g > 188.4$ mm are not included in the manuscript.)

Figs. 9(a)-(b) respectively show the simulated and measured *xy*- and *xz*-plane radiation patterns of Structure B at 5.5 GHz, given $R_g = 18.4$ mm. The *xy*- and *xz*-plane radiation patterns are omnidirectional. In Fig. 9(b), the HPBW is 73°; and the XPL in the azimuth and elevation angles, relative to the LHCP, are less than -15 dB. Figs. 9(c)-(d) show the simulated radiation patterns of Structure B in the *xy*- and *xz*-plane. The simulations were performed with two different ground plane sizes: 109.0 mm ($\cong 2.0\lambda_c$ and 18.4 mm (optimal size). The results indicate that the radiation patterns in *xy*- and *xz*-plane are omnidirectional, with XPL of less than -15 dB. The size of the ground plane (R_g) exerts minimal impact on the radiation pattern.

Figs. 9(e)-(f) show the simulated and measured *xy*- and *xz*-plane radiation patterns, given $R_g = 119.2$ mm ($\cong 2.15\lambda$ *xy*- and *xz*-plane radiation patterns ($R_g = 119.2$ mm) are omnidirectional with XPL < -15 dB.

Figs. 9(g)-(h) show the simulated and measured *xy*- and *xz*-plane radiation patterns, given $R_g = 188.4$ mm. The simulation and measured results are in good agreement. The *xy*- and *xz*-plane radiation patterns are near-omnidirectional with XPL < -10 dB.

As seen in Figs. 9(a)-(h), the *xy*- and *xz*-plane radiation patterns are omnidirectional, independent of R_g(18.4 –188.4 mm). Meanwhile, in Figs. 9(e)-(h), the elevation angle (θ) of the main beam direction and the minimum XPL tilt upward to 75° from originally 90°. To achieve XPL ≤ -15 dB and the elevation angle (θ) of or close to 90°,
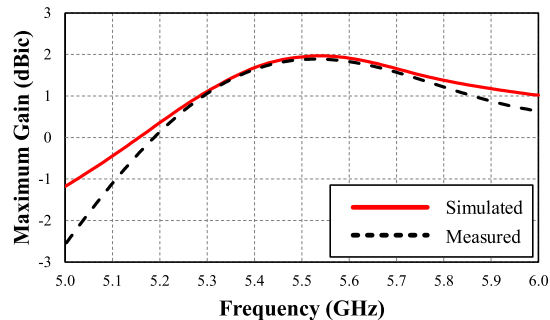
(a)

(b)

FIGURE 10. Simulated and measured AR of Structure B: (a) R_g = 18.4 mm at (θ, ϕ) = (90°, 0°), (b) R_g = 18.4 mm at (θ, ϕ) = (90°, 0°) and R_g = 109.0 to 188.4 mm at (θ, ϕ) = (75°, 0°).

FIGURE 11. Simulated and measured maximum antenna gains of Structure B at (θ, ϕ) = (80°, 0°), given R_g = 18.4 mm.

R_g is between 18.4 –188.4 mm. With R_g = 18.4 –188.4 mm, the radiation pattern of Structure B is circularly polarized.

Fig. 10(a) shows the simulated and measured AR of Structure B at (θ, ϕ) = (90°, 0°), given R_g = 18.4 mm. The simulated and measured AR bandwidth (AR ≤ 3 dB) cover 5.38 – 5.62 GHz and 5.36 – 5.60 GHz, respectively. The simulated and measured results are in good agreement. Fig. 10(b) shows the simulated and measured AR at (θ, ϕ) = (90°, 0°) given R_g = 18.4 mm; and at (θ, ϕ) = (75°, 0°) under variable R_g (109.0 – 188.4 mm). (Note: the minimum AR are achieved at the elevation and azimuth angles (θ, ϕ) of 90°, 0° for R_g = 18.4 mm and at (θ, ϕ) = (75°, 0°) for R_g = 109.0 – 188.4 mm.)

In Fig. 10(b), the AR frequency, given AR ≤ 3 dB, shifts from 5.5 to 5.6 GHz as R_g increases from 18.4 to 188.4 mm. The enlargement of R_g shifts the AR frequency higher (deviating from the target frequency of 5.5 GHz) although the AR level is generally below 3 dB. The enlarged ground plane size (R_g) has an effect on the AR frequency and AR level. The simulated and measured results are in reasonable agreement (Fig. 10(b)). To achieve AR ≤ 3 dB and the omnidirectional radiation pattern, R_g of Structure B must be between 18.4(0.34λ_c) − 188.4 mm (3.5λ_c). Evidently, the ground plane size (R_g) of Structure B is more flexible than Structure A (i.e., R_g of Structure A remains fixed at 39.2 mm).

In Fig. 10(b), the AR frequency remains relatively unchanged as R_g increases from 109.0 mm to 188.4 mm. On the other hand, the minimum AR vary, depending on R_g. The results indicate that the enlarged bottom ground plane

size (R_g = 109.0 − 188.4 mm) has a negligible effect on the AR frequency. For R_g > 188.4 mm, AR deteriorates (i.e., AR > 3 dB) as the ground plane enlargement significantly magnifies the magnitude of the horizontal component of circular polarization, resulting in disproportionate magnitudes between the horizontal and vertical components. For very large R_g (> 188.4 mm), multi-ring structures (e.g., triple- or quadruple-ring) could be used to overcome the AR deterioration.

Fig. 11 shows the simulated and measured maximum antenna gains of Structure B at (θ, ϕ) = (80°, 0°), given R_g = 18.4 mm. (Note: The maximum antenna gain is achieved at the elevation and azimuth angles of 80° and 0°, respectively.) The simulated and measured results are in good agreement, with the simulated and measured maximum antenna gains at 5.5 GHz of 2.0 and 1.96 dBic, respectively.

In essence, the OCPA with SA-AMC ground plane (Structure B) circumvents the design rigidity as the bottom ground plane size (R_g) could be varied between 18.4 − 188.4 mm, without affecting the impedance and AR bandwidths and omnidirectionality of the antenna scheme. Besides, the experimental results of Structure B with aluminum installation base (corresponding to an expanded bottom ground plane) of different radii (119.2 and 188.4 mm), given the bottom ground plane radius (R_g) of 18.4 mm, show that the installation base has no effect on the impedance and AR bandwidths and omnidirectionality of OCPA. However, the measured $|S_{11}|$ (8.08%) and AR bandwidths (4.38%) of Structure B (without the aluminum installation base) are still unsatisfactory. As a result, the subsequent sub-section proposes the OCPA with DA-AMC ground plane (Structure C).

B. CIRCULARLY POLARIZED OMNIDIRECTIONAL MONOPOLE ANTENNA WITH DA-AMC (STRUCTURE C)

To further enhance the $|S_{11}|$ and AR bandwidths, the SA-AMC (Structure BC. Fig. 12 shows the prototype of Structure C (i.e., the OCPA with DA-AMC ground plane).

Fig. 13 shows the simulated reflection phase of the DA-AMC ground plane of Structure C. Fig 13(a) shows the simulated reflection phases in the x- and y-polarizations. Both reflection phases are almost identical. The substitution of the SA-AMC with DA-AMC ground plane enhances the
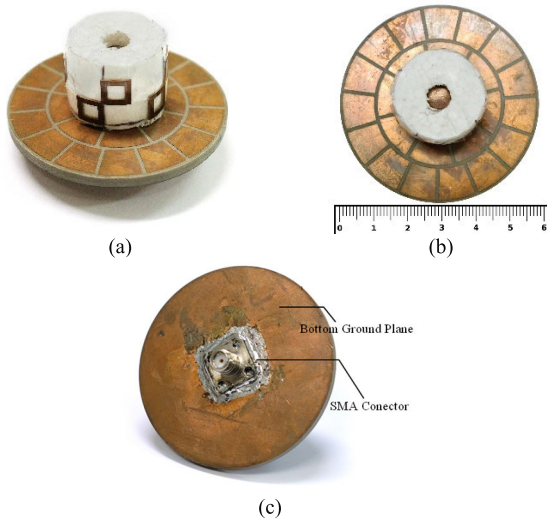
FIGURE 12. Prototype of Structure C: (a) Perspective view, (b) Top view, (d) Bottom view.
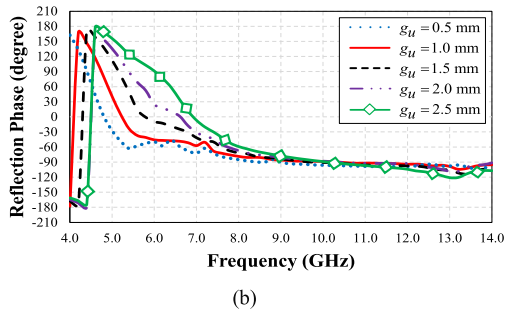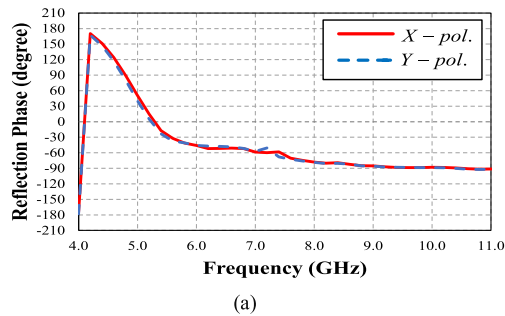

FIGURE 13. Simulated reflection phase of the DA-AMC ground plane of Structure C : (a) in the x- and y-polarizations, (b) the effect of gap width (g_u) on the AMC reflection phase.

reflection phase bandwidth (AMC band) by 51.37%, from 24.13% (Structure B) to 75.50% (Structure C), covering 4.7 – 10.4 GHz.

Fig. 13(b) shows the effect of gap width (g_u) on the AMC reflection phase: g_u = 0.5, 1.0, 1.5, 2.0, and 2.5 mm. As g_u increases, the center frequency (where the reflection phase = 0°) shifts to higher frequency, deviating from the target frequency of 5.5 GHz. Besides, the reflection phase bandwidth fails to cover the lower frequency band as g_u becomes larger [33].

Fig. 14 shows the effect of variable bottom ground plane radii (R_g) on the impedance bandwidth ($|S_{11}| \leq -10$ dB) of Structure C. Specifically, Fig. 14(a) shows the simulated and
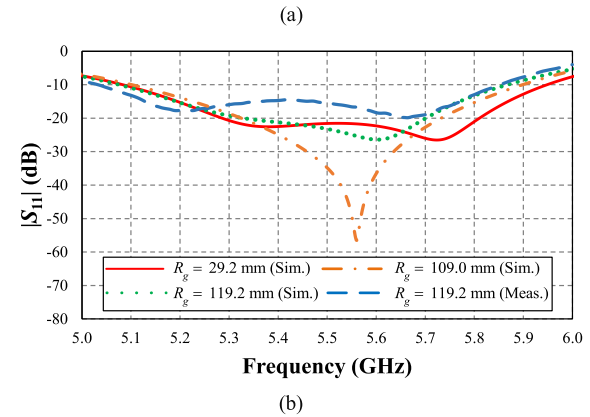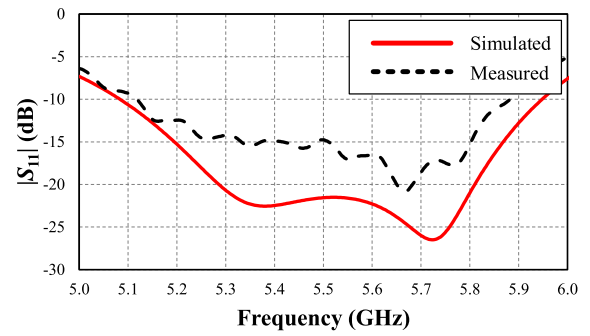

FIGURE 14. Simulated and measured $|S_{11}|$ of Structure C under variable bottom ground plane radii (R_g): (a) the optimal R_g of 29.2 mm, (b) variable R_g.

measured $|S_{11}|$ bandwidths, given the optimal R_g = 29.2 mm. The simulated and measured $|S_{11}|$ bandwidth cover 5.08 – 5.95 GHz (15.77%) and 5.11 – 5.89 GHz (14.36%), respectively. The DA-AMC structure enhances the $|S_{11}|$ bandwidth of OCPA, vis-à-vis the SA-AMC (Fig. 8) and the conventional OCPA (Fig. 4).

Fig. 14(b) shows the simulated and measured impedance bandwidths ($|S_{11}| \leq -10$ dB) of Structure C under variable R_g. The results indicate that the enlargement of R_g has a minimal effect on the impedance bandwidth. The finding could be attributed to the reduced leakage current on the coaxial feeder cable due to the DA-AMC structure.

Figs. 15(a)-(b) show the simulated and measured radiation patterns of Structure C in xy- and xz-planes, given the optimal R_g = 29.2 mm (Table 2). The xy- and xz-plane radiation patterns are omnidirectional. In Fig. 15(b), HPBW of Structure C is 82°, and the minimal XPL in the azimuth and elevation angles, relative to the LHCP, are less than –15 dB.

Figs. 15(c)-(d) show, as an example, the simulated radiation patterns in xy- and xz-planes of Structure C, given R_g = 29.2 and 109.0 mm ($\cong 2.0\lambda$). The results show that the radiation patterns vary, depending on the bottom ground plane size (R_g). The xy- and xz-plane radiation patterns are omnidirectional with XPL < –15 dB at $\theta = 80°$, given R_g = 109.0 mm ($\cong 2.0\lambda$).

Figs. 15(e)-(f) show the simulated and measured xy- and xz-plane radiation patterns, given R_g = 119.2 mm ($\cong 2.15\lambda_c$).
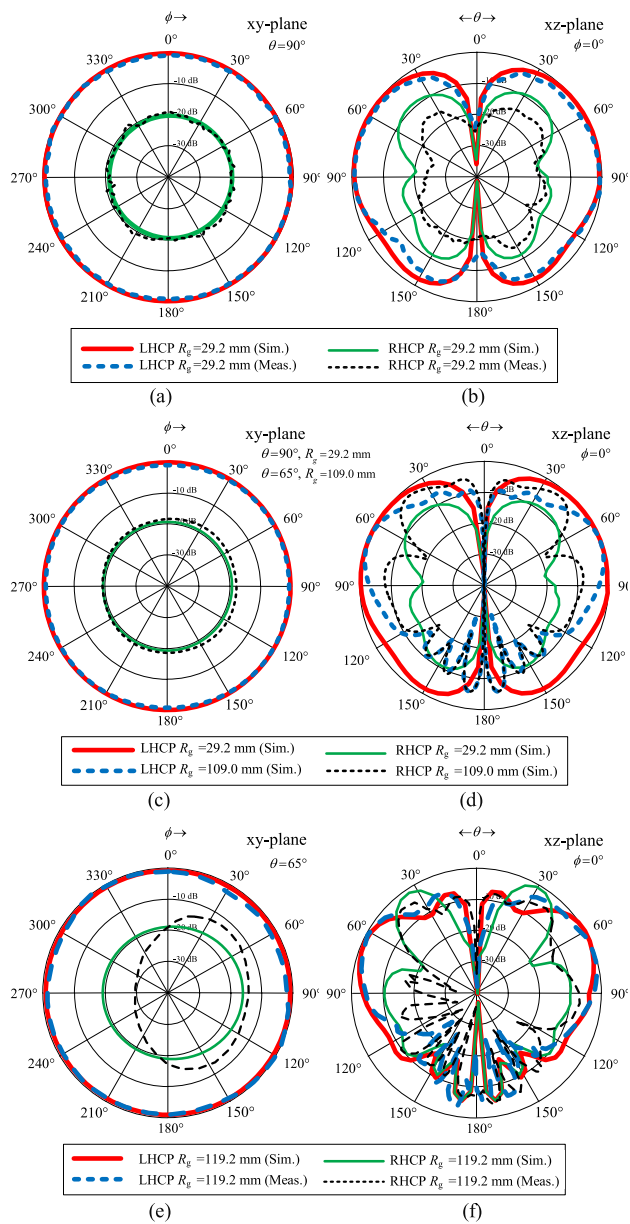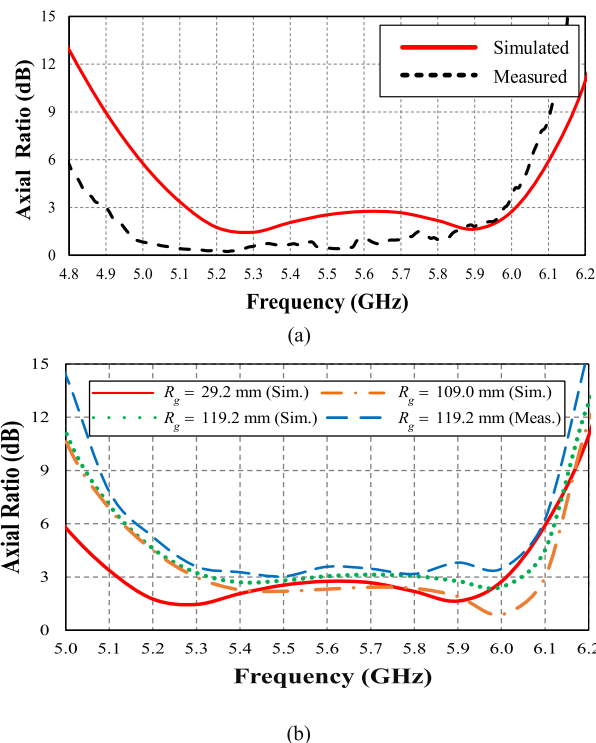
FIGURE 15. Simulated and measured radiation patterns of Structure C given the target center frequency of 5.5 GHz: (a) *xy*-plane for R_g= 29.2 mm (0.54λc), (b) *xz*-plane for R_g = 29.2 mm (0.54λc), (c) *xy*-plane for R_g = 29.2 mm (0.54λc) and 109.0 mm ($\cong$2λc), (d) *xz*-plane for R_g = 29.2 mm (0.54λc) and 109.0 mm ($\cong$2λc), (e) *xy*-plane for R_g = 119.2 mm ($\cong$2.15λc), (f) *xz*-plane for R_g = 119.2 mm ($\cong$2.15λc).

The simulated and measured results are in reasonable agreement. The *xy*- and *xz*-plane radiation patterns are near-omnidirectional with XPL < − 15 dB at θ = 65°.

As shown Figs. 15(a)-(f), the *xy* and *xz*-plane radiation patterns of Structure C are omnidirectional, given that R_g = 29.2 – 119.2 mm (0.54λ_c – 2.15λ_c). The elevation angle (θ) of the main beam direction and the minimum XPL in the *xz* plane tilt upward from 80° to 65° as R_g increases. To achieve XPL $\leq$ − 15 dB and the elevation angle (θ) of or close to 90°, R_g of Structure C must be between 29.2 –119.2 mm (0.54λ_c – 2.15λ_c).
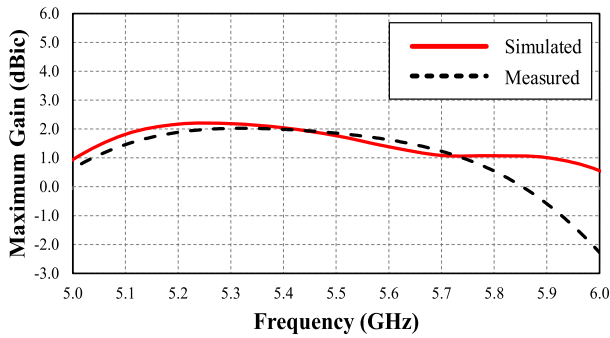

FIGURE 16. Simulated and measured AR of Structure C: (a) R_g = 29.2 mm at (θ, ϕ) = (90°, 0°), (b) R_g = 109.0 − 119.2 mm at (θ, ϕ) = (65°, 0°). (Note: the minimum AR are achieved at the elevation and azimuth angles (θ, ϕ) of 90°, 0° for R_g = 29.2 mm and at (θ, ϕ) = (65°, 0°) for R_g = 109.0 – 119.2 mm.)

Fig. 16(a) shows the simulated and measured AR of Structure C at (θ, ϕ) = (90°, 0°), given the optimal R_g = 29.2 mm. The simulated and measured AR bandwidth (AR $\leq$ 3 dB) cover 5.12 – 6.01 GHz and 4.90 – 5.98 GHz, respectively. The simulated and measured results are in reasonable agreement. Compared to Structures A and B, Structure C achieves wider simulated and measured AR bandwidths of 15.87% and 16.24%, respectively. The enhanced AR bandwidth could be attributed the DA-AMC ground plane.

Fig. 16(b) shows the simulated and measured AR of Structure C at (θ, ϕ) = (65°, 0°) under variable R_g (between 29.2 and 119.2 mm). The AR frequency (AR $\leq$ 3 dB) shifts to higher frequency as R_g increases from 29.2 to 119.2 mm. Specifically, the enlargement of the ground plane has an effect on the AR level and AR frequency. To achieve AR $\leq$ 3 dB and omnidirectionality, R_g must be less than or equal to 2λ_c (109.0 mm). In the figure, the measured AR, given R_g = 119.2 mm, has the similar pattern to that of the simulated AR despite the deteriorating measured AR (AR $\geq$ 3 dB). The AR deterioration could be attributed to the antenna fabrication and discrepancy between the simulation and measurement angles. In comparison, Structure C, given R_g = 29.2 – 119.2 mm (2.15λ_c), could achieve wider AR bandwidth (AR $\leq$ 3 dB) than Structures A and B.

Meanwhile, the experimental results of Structure C with aluminum installation base of different radii (119.2 and 188.4 mm), given the bottom ground plane radius (R_g) of

FIGURE 17. Simulated and measured maximum antenna gains of Structure C at $(\theta, \phi) = (80°, 0°)$, given R_g = 29.2 mm.
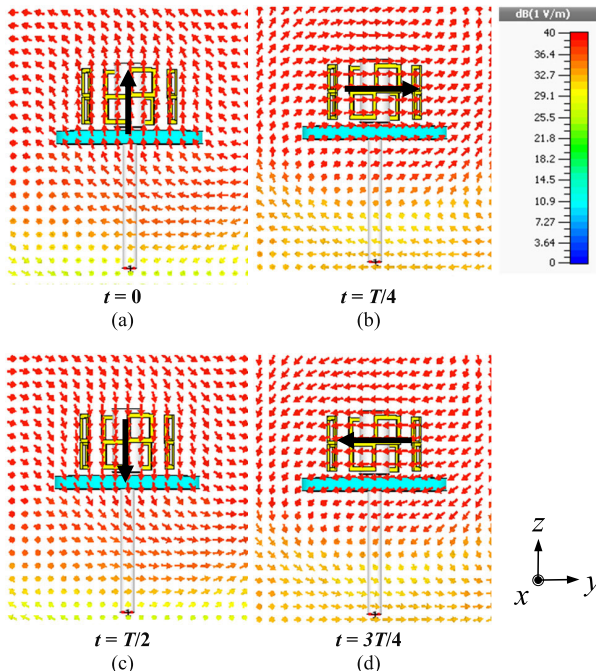
FIGURE 18. Electric field distribution of Structure B at: (a) $t = 0$, (b) $t = T/4$, (c) $t = T/2$, (d) $t = 3T/4$, where T is the period of oscillation at 5.5 GHz.
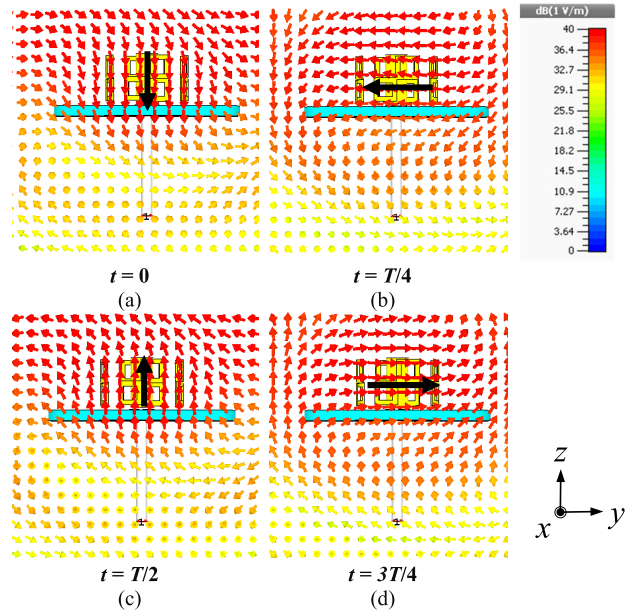

FIGURE 19. Electric field distribution of Structure C at: (a) $t = 0$, (b) $t = T/4$, (c) $t = T/2$, (d) $t = 3T/4$, where T is the period of oscillation at 5.5 GHz.

FIGURE 20. Electric field distribution in TM_{21} mode of Structure B: a) 5.05 GHz, b) 5.5 GHz, c) 6.0 GHz.

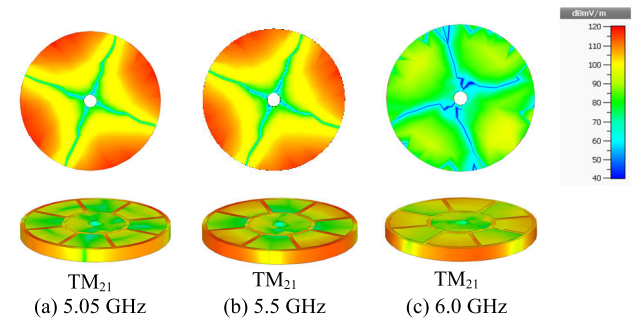29.2 mm, demonstrate that the installation base has no effect on the impedance and AR bandwidths and omnidirectionality of OCPA.

Fig. 17 shows the simulated and measured antenna gains of Structure C at $(\theta, \phi) = (80°, 0°)$ given R_g = 29.2 mm (optimal). (Note: The maximum antenna gain is achieved at the elevation and azimuth angles of 80° and 0°, respectively.) The simulated and measured results are in good agreement. By comparison, the maximum antenna gain of Structure C (2.18 dBic) is higher than Structure B (1.96 dBic). This could be attributed to the broader impedance ($|S_{11}| \leq -10$ dB) and AR (≤ 3 dB) bandwidths of Structure C.

V. EFFECT OF AMC ON CIRCULAR POLARIZATION AND COMPARISON BETWEEN PROPOSED AMC STRUCTURES AND CONVENTIONAL OCPA

To investigate the effects of different AMC ground planes on the CP characteristics and leakage current, this section investigates the electric field distribution in the reactive near-field region of the OCPAs with SA- (Structure B) and DA-AMC ground planes (Structure C).

Figs. 18(a)-(d) show the electric field distribution of Structure B at four different time points in one cycle of T, where T is the period of oscillation at 5.5 GHz. The electric field rotates clockwise with constant electric field magnitude, resulting in circular polarization. Likewise, in Figs. 19(a)-(d), the electric field of Structure C rotates clockwise with constant electric field magnitude, giving rise to circular polarization.

As shown in Figs. 18 and 19, the electric field surrounding the SA- and DA-AMC ground planes is of vertical ($t = 0$ and $t = T/2$) and horizontal ($t = T/4$ and $t = 3T/4$) components, resulting in circular polarization. Essentially, the SA- and DA-AMC ground planes enhance the AR bandwidth, resulting in wider CP radiation, vis-à-vis Structure A. The wider CP radiation could be attributed to the horizontal electric field on the surface of the AMC ground planes. Specifically, the reflection phase bandwidth of the DA-AMC structure
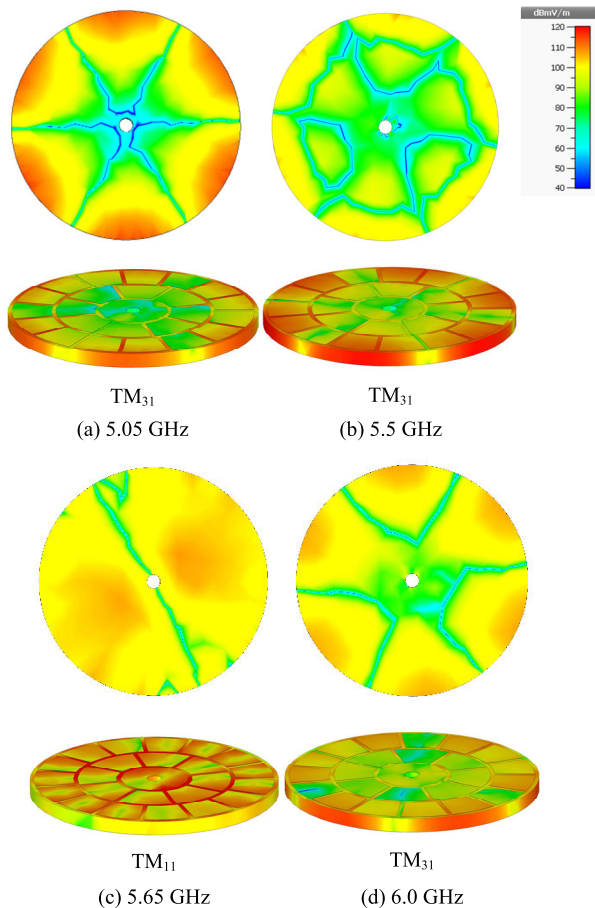
FIGURE 21. Electric field distribution in TM_{31} and TM_{11} modes of Structure C: (a) TM_{31} mode at 5.05 GHz, (b) TM_{31} mode at 5.5 GHz, (c) TM_{11} mode at 5.65 GHz, (d) TM_{31} mode at 6.0 GHz.

TM$_{31}$ (a) 5.05 GHz

TM$_{31}$ (b) 5.5 GHz

TM$_{11}$ (c) 5.65 GHz

TM$_{31}$ (d) 6.0 GHz
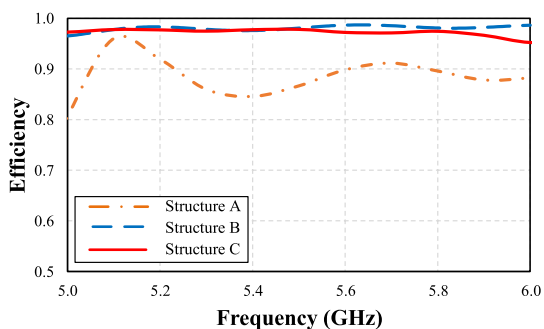
FIGURE 22. Simulated radiation efficiency of Structures A, B and C, given the optimal R_g = 39.2, 18.4 and 29.2 mm for Structures A, B and C, respectively.

is wider than that of the SA-AMC, resulting in wider AR bandwidth and wider CP radiation. However, in the absence of the SA-AMC or DA-AMC structures (i.e., Structure A), there exists only the vertical electric field on the conductor ground plane, giving rise to narrow circular polarization and AR deterioration.

Figs. 20 (a)-(c) show the electric field distribution of Structure B in TM_{21} mode at 5.05, 5.5, and 6.0 GHz. At 5.5 GHz, strong electric fields are observed on almost all sides of the
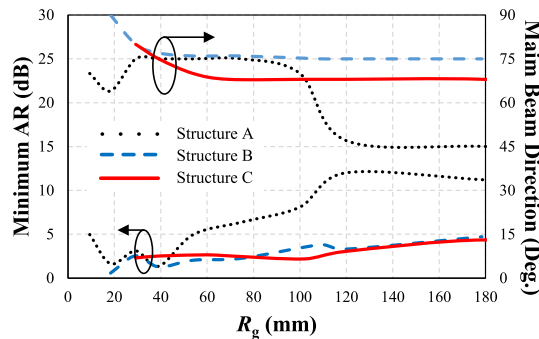
FIGURE 23. Simulated minimum AR and the corresponding elevation angles (θ) of Structures A, B and C in relation to the bottom ground plane radii (R_g).
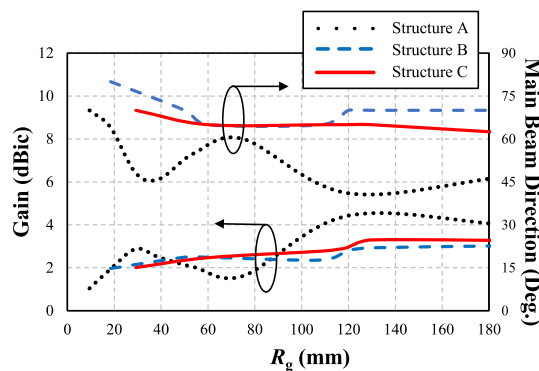
FIGURE 24. Simulated gains and the elevation angles (θ) of Structures A, B and C in relation to the bottom ground plane radii (R_g) at 5.5 GHz.

TABLE 3. Simulated results of the conventional OCPA (Structure A) and the proposed OCPA with AMC (Structure B and C).

Structu-res	|S_{11}| bandwidth (%)	ARBW (%)	XPL (dB) xy-plane	XPL (dB) xz-plane	Elevation of θ for min. AR	Gain	R_g Radius for CP
A	4.68	4.49	-12.70	-12.70	90°	2.49 dBic	$0.72\lambda_c$
B	5.99	4.38	-34.73	-34.57	90°	1.96 dBic	$0.34\lambda_c - 3.5\lambda_c$
C	15.77	15.99	-20.36	-20.62	80°	2.18 dBic	$0.54\lambda_c - 2.15\lambda_c$

AMC structure. At 5.05 GHz, the electric fields around the AMC structure become less strong. At 6.0 GHz, the electric field strength is significantly reduced. As a result, Structure B resonates in TM_{21} mode [34], resulting in narrower impedance and AR bandwidths, compared to Structure C.

Figs. 21(a)-(d) show the electric field distribution of Structure C in TM_{31} and TM_{11} modes. The TM_{31} mode exhibits a wideband resonance, with strong electric fields propagating on the AMC structure at 5.05 GHz, 5.5 GHz, and 6.0 GHz. On the other hand, the TM_{11} mode resonates at 5.65 GHz, where strong electric fields are observed on both sides of the AMC structure. The concurrent presence of both TM_{31} and TM_{11} modes [34] in Structure C contributes to broader impedance and AR bandwidths, in comparison with Structure B.

TABLE 4. Comparison between the performance of the existing OCPAs and the proposed antennas.

References	$\lvert S_{11}\rvert$ bandwidth (%)	AR bandwidth (%)	Maximum gain (dBic)	Center frequency (GHz)	Balun requirement	Occurrence of non-omnidirectionality when in direct contact with installation base	Overall antenna dimensions
[1]	19.84% 2.27-2.77GHz	17.67% 2.27-2.71 GHz	3.75	2.49 GHz	yes	yes	$1.362\lambda_L \times 1.362\lambda_L \times 0.023\lambda_L$ at 2.27 GHz
[3]	13.17% 2.34-2.67 GHz	10.50% 2.26-2.51 GHz	1.12	2.38 GHz	yes	yes	$0.390\lambda_L \times 0.390\lambda_L \times 0.156\lambda_L$ at 2.34 GHz
[11]	9.00% 2.32-2.54 GHz	11.76% 2.32-2.61 GHz	1.20	2.43 GHz	no	yes	$0.255\lambda_L \times 0.255\lambda_L \times 0.155\lambda_L$ at 2.32 GHz
[12]	4.48% 2.40-2.51 GHz	1.21% 2.46-2.48 GHz	1.90	2.47 GHz	yes	yes	$0.640\lambda_L \times 0.368\lambda_L \times 0.048\lambda_L$ at 2.40 GHz
[13]	24.42% 2.30-2.94 GHz	7.25% 2.39-2.57 GHz	0.91	2.48 GHz	yes	yes	$0.299\lambda_L \times 0.299\lambda_L \times 0.253\lambda_L$ at 2.30 GHz
[14]	10.40% 2.37-2.63 GHz	8.90% 2.36-2.58 GHz	1.56	2.47 GHz	yes	yes	$0.418\lambda_L \times 0.418\lambda_L \times 0.158\lambda_L$ at 2.37 GHz
[23]	9.37% 2.34-2.57 GHz	8.00% 2.40-2.60GHz	2.07	2.48 GHz	yes	yes	$0.407\lambda_L \times 0.407\lambda_L \times 0.438\lambda_L$ at 2.35 GHz
Structure B*	**8.08% 5.34-5.79 GHz**	**4.38% 5.36-5.60 GHz**	**1.96**	5.48 GHz	**no**	**no**	$0.655\lambda_L \times 0.655\lambda_L \times 0.363\lambda_L$ at 5.34 GHz
Structure C**	**14.37% 5.08-5.89 GHz**	**19.85% 4.90-5.98 GHz**	**2.18**	5.50 GHz	**no**	**no**	$0.982\lambda_L \times 0.982\lambda_L \times 0.333\lambda_L$ at 5.08 GHz

Note:　　　 * In Structure B, the minimum AR is achieved at $(\theta, \phi) = (90°, 0°)$, and the optimal bottom ground plane $(R_g) = 18.4$ mm.

　　　　　　 ** In Structure C, the minimum AR is achieved at $(\theta, \phi) = (90°, 0°)$, and the optimal bottom ground plane $(R_g) = 29.2$ mm.

　　　 λ_L: the free-space wavelength corresponding to the lowest operating frequency of the antenna.

Fig. 22 compares the simulated radiation efficiency of Structures A, B and C at their respective optimal R_g (i.e., the optimal R_g = 39.2, 18.4, and 29.2 mm for Structures A, B, and C). The radiation efficiency of Structure A is poorer than that of Structures B and C. The poorer radiation efficiency of Structure A is attributable to larger non-AMC ground plane size (R_g). Essentially, the AMC structures stabilize and enhance the radiation efficiency of OCPA.

Figure 23 shows the simulated minimum AR and the corresponding elevation angles (θ) of Structures A, B, and C relative to R_g. In Structure A, the minimum AR is less than 3 dB (AR $\leq$ 3 dB) if $15 \leq R_g \leq 45$ mm, with the corresponding θ of $65° - 75°$. In Structure B (the OCPA with SA-AMC), the enlargement of R_g results in non-circular polarization as the minimum AR > 3 dB, with the elevation angle (θ) tilting upward from 90° to 75°. In Structure C, the enlargement of R_g also results in non-circular polarization as the minimum AR > 3 dB, with θ tilting upward from 90° to 65°. Essentially, the integration of the AMC structure with OCPA circumvents the design rigidity as the bottom ground plane radius (R_g) can be varied between 18.4 – 188.4 mm for Structure B and between 29.2 – 119.2 mm for Structure C (without affecting the omnidirectionality and the impedance and AR bandwidths), vis-à-vis the fixed R_g of Structure A (39.2 mm).

Figure 24 shows the simulated gains and elevation angles (θ) of Structures A, B, and C relative to R_g at 5.5 GHz. In Structure A, the gain is less than 2.0 dBic when $R_g \leq 20$ mm and between $55 – 80$ mm, with θ of $37° - 78°$. In structure B, the enlargement of R_g increases the gain (> 2.0 dBic) when R_g > 20 mm, with θ tilting upward from 80° to 65°. In Structure C, the enlargement of R_g also enhances the gain (> 2.0 dBic) when R_g > 29.2 mm, with θ tilting upward from 70° to 64°. In relation to Structure A (without the AMC), the antenna gains of Structures B and C (with the AMC structures) become more stable.

Table 3 summarizes the characteristics and simulated performance of Structures A, B and C. By comparison, the proposed omnidirectional CP antenna with DA-AMC ground plane (Structure C) outperforms the rest in terms of the impedance (15.77%) and AR bandwidths (15.99%) and antenna gain (2.18 dBic). Specifically, the ARBW of Structures A and B are insignificantly different. Nevertheless, Structure A encounters the design rigidity as the bottom ground plane radius (R_g) remains fixed (39.2 mm), while Structure B possesses the design flexibility as R_g could be varied between 18.4 – 188.4 mm, without affecting the omnidirectionality and the impedance and AR bandwidths. In Structure C, the $\lvert S_{11}\rvert$ and AR bandwidths are substantially enhanced. Besides, Structure C provides antenna developers with design flexibility as R_g could be varied between 29.2 – 119.2 mm, with wider $\lvert S_{11}\rvert$ and AR bandwidths and omnidirectional radiation pattern.

Table 4 compares the performance of the existing OCPAs (i.e., conventional OCPAs) and the proposed OCPA with SA- (Structure B) and DA-AMC ground plane (Structure C).

VI. CONCLUSION

This research proposes the OCPAs with SA-AMC and DA-AMC ground planes for IoT applications, such as intelligent transport systems and vehicle-to-vehicle communication. The OCPA with SA-AMC ground plane (Structure B) consists of a monopole element, four diagonally adjoined parasitic elements and an SA-AMC ground plane, while the OCPA with DA-AMC ground plane (Structure C) consists of a monopole element, four diagonally adjoined parasitic elements, and a DA-AMC ground plane. Unlike the conventional OCPA (Structure A with fixed bottom ground plane radius (R_g) of 39.2 mm), R_g of Structures B and C can be varied between 18.4 – 188.4 mm; and 29.2 – 119.2 mm, respectively, without affecting the omnidirectionality and impedance and AR bandwidths. The measured impedance and AR bandwidths of Structure B, given the optimal R_g of 18.4 mm, are 8.08% (5.34 –5.79 GHz) and 4.38% (5.36 –5.60 GHz), while those of Structure C, given the optimal R_g of 29.2 mm, are 14.37% (5.08 –5.89 GHz) and 19.85% (4.90 –5.98 GHz). Future work will experimentally implement the proposed AMC-based OCPA on various conductive installation bases of actual size to determine their effect of the conductive bases on the omnidirectionality, impedance and AR bandwidths, and gain of the antenna scheme.

REFERENCES

[1] Y. M. Pan, S. Y. Zheng, and B. J. Hu, "Wideband and low-profile omnidirectional circularly polarized patch antenna," *IEEE Trans. Antennas Propag.*, vol. 62, no. 8, pp. 4347–4351, Aug. 2014.

[2] Y. M. Pan and K. W. Leung, "Wideband omnidirectional circularly polarized dielectric resonator antenna with parasitic strips," *IEEE Trans. Antennas Propag.*, vol. 60, no. 6, pp. 2992–2997, Jun. 2012.

[3] W. W. Li and K. W. Leung, "Omnidirectional circularly polarized dielectric resonator antenna with top-loaded Alford loop for pattern diversity design," *IEEE Trans. Antennas Propag.*, vol. 61, no. 8, pp. 4246–4256, Aug. 2013.

[4] B. Li and Q. Xue, "Polarization-reconfigurable omnidirectional antenna combining dipole and loop radiators," *IEEE Antennas Wireless Propag. Lett.*, vol. 12, pp. 1102–1105, 2013.

[5] Y. Shi and J. Liu, "Wideband and low-profile omnidirectional circularly polarized antenna with slits and shorting-vias," *IEEE Antennas Wireless Propag. Lett.*, vol. 15, pp. 686–689, 2016.

[6] Y.-M. Cai, S. Gao, Y. Yin, W. Li, and Q. Luo, "Compact-size low-profile wideband circularly polarized omnidirectional patch antenna with reconfigurable polarizations," *IEEE Trans. Antennas Propag.*, vol. 64, no. 5, pp. 2016–2021, May 2016.

[7] Y. Yu, Z. Shen, and S. He, "Compact omnidirectional antenna of circular polarization," *IEEE Antennas Wireless Propag. Lett.*, vol. 11, pp. 1466–1469, 2012.

[8] D. Yu, S.-X. Gong, Y.-T. Wan, Y.-L. Yao, Y.-X. Xu, and F.-W. Wang, "Wideband omnidirectional circularly polarized patch antenna based on vortex slots and shorting vias," *IEEE Trans. Antennas Propag.*, vol. 62, no. 8, pp. 3970–3977, Aug. 2014.

[9] X. Quan, R. Li, and M. M. Tentzeris, "A broadband omnidirectional circularly polarized antenna," *IEEE Trans. Antennas Propag.*, vol. 61, no. 5, pp. 2363–2370, May 2013.

[10] B. Yektakhah and K. Sarabandi, "A wideband circularly polarized omnidirectional antenna based on excitation of two orthogonal circular TE21 modes," *IEEE Trans. Antennas Propag.*, vol. 65, no. 8, pp. 3877–3888, Aug. 2017.

[11] Y. Yu, J. Xiong, and H. Li, "Compact omni-directional circularly polarised antenna utilising bended dipoles and integrated baluns," *IET Microw., Antennas Propag.*, vol. 11, no. 10, pp. 1409–1414, Jul. 2017.

[12] A. Narbudowicz, X. Bao, M. Ammann, H. Shakhtour, and D. Heberling, "Circularly polarized antenna with steerable dipole-like radiation pattern," *IEEE Trans. Antennas Propag.*, vol. 62, no. 2, pp. 519–526, Feb. 2014.

[13] Y. M. Pan, K. W. Leung, and K. Lu, "Omnidirectional linearly and circularly polarized rectangular dielectric resonator antennas," *IEEE Trans. Antennas Propag.*, vol. 60, no. 2, pp. 751–759, Feb. 2012.

[14] W. Li, K. W. Leung, and N. Yang, "Omnidirectional dielectric resonator antenna with a planar feed for circular polarization diversity design," *IEEE Trans. Antennas Propag.*, vol. 66, no. 3, pp. 1189–1197, Mar. 2018.

[15] K. Lertsakwimarn, C. Phongcharoenpanich, and T. Fukusako, "Design of circularly polarized and electrically small antenna with omnidirectional radiation pattern," *IEICE Trans. Commun.*, vol. E97, 12, pp. 2739–2746, Dec. 2014.

[16] J. Wu, S. Yang, Y. Chen, S. Qu, and Z. Nie, "A low profile dual-polarized wideband omnidirectional antenna based on AMC reflector," *IEEE Trans. Antennas Propag.*, vol. 65, no. 1, pp. 368–374, Jan. 2017.

[17] Q.-X. Chu, M. Ye, and X.-R. Li, "A low-profile omnidirectional circularly polarized antenna using planar sector-shaped endfire elements," *IEEE Trans. Antennas Propag.*, vol. 65, no. 5, pp. 2240–2247, May 2017.

[18] J. Wu and K. Sarabandi, "Compact omnidirectional circularly polarized antenna," *IEEE Trans. Antennas Propag.*, vol. 65, no. 4, pp. 1550–1557, Apr. 2017.

[19] L. Peng, K. Sun, X. Jiang, S.-M. Li, and C.-L. Ruan, "EZR-MZR resonators for compact low-profile omnidirectional circular-polarized antenna design," *IEEE Photon. J.*, vol. 9, no. 4, pp. 1–15, Aug. 2017.

[20] W. Cao, "Compact dual-band dual-mode circular patch antenna with broadband unidirectional linearly polarised and omnidirectional circularly polarised characteristics," *IET Microw., Antennas Propag.*, vol. 10, no. 2, pp. 223–229, Jan. 2016.

[21] B. Zhou, J. Geng, X. Bai, L. Duan, X. Liang, and R. Jin, "An omnidirectional circularly polarized slot array antenna with high gain in a wide bandwidth," *IEEE Antennas Wireless Propag. Lett.*, vol. 14, pp. 666–669, 2015.

[22] S. Karki, M. Sabbadini, K. Alkhalifeh, and C. Craeye, "Metallic monopole parasitic antenna with circularly polarized conical patterns," *IEEE Trans. Antennas Propag.*, vol. 67, no. 8, pp. 5243–5252, Aug. 2019.

[23] P. Dangkham, S. Dentri, C. Phongcharoenpanich, and P. Akkaraekthalin, "Circularly polarized omnidirectional antenna with dipole core and diagonally adjoined parasitic braces for ISM band applications," *Int. J. Antennas Propag.*, vol. 2019, Aug. 2019, Art. no. 2463871.

[24] D. Feng, H. Zhai, L. Xi, S. Yang, K. Zhang, and D. Yang, "A broadband low-profile circular-polarized antenna on an AMC reflector," *IEEE Antennas Wireless Propag. Lett.*, vol. 16, pp. 2840–2843, 2017.

[25] A. Jafargholi, M. Kamyab, and M. Veysi, "Artificial magnetic conductor loaded monopole antenna," *IEEE Antennas Wireless Propag. Lett.*, vol. 9, pp. 211–214, 2010.

[26] A. Foroozesh and L. Shafai, "Investigation into the application of artificial magnetic conductors to bandwidth broadening, gain enhancement and beam shaping of low profile and conventional monopole antennas," *IEEE Trans. Antennas Propag.*, vol. 59, no. 1, pp. 4–20, Jan. 2011.

[27] H. H. Tran and I. Park, "A dual-wideband circularly polarized antenna using an artificial magnetic conductor," *IEEE Antennas Wireless Propag. Lett.*, vol. 15, pp. 950–953, 2016.

[28] W. Lin, S.-L. Chen, R. W. Ziolkowski, and Y. J. Guo, "Reconfigurable, wideband, low-profile, circularly polarized antenna and array enabled by an artificial magnetic conductor ground," *IEEE Trans. Antennas Propag.*, vol. 66, no. 3, pp. 1564–1569, Mar. 2018.

[29] J. Sarrazin, A.-C. Lepage, and X. Begaud, "Circular high-impedance surfaces characterization," *IEEE Antennas Wireless Propag. Lett.*, vol. 11, pp. 260–263, 2012.

[30] M. A. Amiri, C. A. Balanis, C. R. Birtcher, and G. C. Barber, "Curvilinear antennas above a spherical HIS," *IEEE Trans. Antennas Propag.*, vol. 68, no. 10, pp. 7208–7213, Oct. 2020.

[31] M. Tanabe and H. Nakano, "Low-profile wideband spiral antenna with a circular HIS reflector composed of homogeneous fan-shaped patch elements," *IEEE Trans. Antennas Propag.*, vol. 68, no. 10, pp. 7219–7222, Oct. 2020.

[32] J. Zhang, S. Yan, and G. A. E. Vandenbosch, "A multistandard antenna based on a 2-D CRLH-TL in polar coordinates," *IEEE Antennas Wireless Propag. Lett.*, vol. 20, no. 3, pp. 332–336, Mar. 2021.

[33] F. Yang and Y. R. Samii, *Electromagnetic Band Gap Structures in Antenna Engineering*, 1st ed. New York, NY, USA: Cambridge Univ. Press, 2009.

[34] F. Mao, T. Li, Y. Shao, J. Yang, and M. Huang, "Orbital angular momentum radiation from circular patches," *Prog. Electromagn. Res. Lett.*, vol. 61, pp. 13–18, 2016, doi: 10.2528/PIERL16012604.

PISIT JANPANGNGERN was born in Lampang, Thailand, in 1991. He received the B.Eng. degree from the Rajamangala University of Technology Thanyaburi, Thailand, in 2015, and the M.Eng. degree from the King Mongkut's Institute of Technology Ladkrabang (KMITL), Thailand, in 2017, where he is currently pursuing the D.Eng. degree. His research interests include omnidirectional circularly polarized antennas, multiple-input, multiple-output (MIMO) antennas, wideband antennas, and metasurfaces.

RYUJI KUSE (Member, IEEE) received the B.E., M.E., and Ph.D. degrees in engineering from the University of Fukui, Fukui, Japan, in 2011, 2013, and 2016, respectively. In 2017, he joined Kumamoto University, Kumamoto, Japan, where he is currently an Associate Professor with the Department of Computer Science and Electrical Engineering. His research interests include metasurfaces, multiple-input, multiple-output (MIMO) antennas, circularly polarized antennas, and their applications. He is a member of the Institute of Electronics, Information and Communication Engineers (IEICE).

CHUWONG PHONGCHAROENPANICH (Member, IEEE) received the B.Eng. (Hons.), M.Eng., and D.Eng. degrees from the King Mongkut's Institute of Technology Ladkrabang (KMITL), Bangkok, Thailand, in 1996, 1998, and 2001, respectively. He is currently a Professor with the Department of Telecommunications Engineering, KMITL, where he is also the Leader of the Innovative Antenna and Electromagnetic Applications Research Laboratory. His research interests include antenna design for various mobile and wireless communications, conformal antennas, and array antenna theory. He is a Senior Member of IEICE and a member of ECTI. He has served as the Chair for the IEEE MTT/AP/ED Thailand Chapter, from 2014 to 2018. He has been on the organizing committee of several international conferences, including the TPC Chair of the 2009 International Symposium on Antennas and Propagation (ISAP 2009) and a TPC Member of ISAP 2012. He was an Associate Editor of *IEICE Transactions on Communications* and *ECTI Transactions on Electrical Engineering, Electronics, and Communications*. He is also an Associate Editor of *IEICE Communications Express*. He is also a Reviewer of many scientific journals, including IEEE TRANSACTIONS ON ANTENNAS AND PROPAGATION, IEEE ACCESS, *IET Microwaves, Antennas and Propagation*, *Electronics Letters*, and *ECTI Transactions*, and many international conferences, including ISAP and APMC. He was on the Board Committee of ECTI Association, from 2008 to 2011 and from 2014 to 2015.

TAKESHI FUKUSAKO (Senior Member, IEEE) received the B.E., M.E., and Ph.D. degrees in engineering from Kyoto Institute of Technology, Kyoto, Japan, in 1992, 1994, and 1997, respectively. In 1997, he joined Kumamoto University, Kumamoto, Japan, as a Research Associate, where he is currently a Professor with the Department of Computer Science and Electrical Engineering. From 2005 to 2006, he was a Visiting Researcher with the University of Manitoba, Winnipeg, MN, Canada. He was a Visiting Associate Professor with the City University of Hong Kong, Hong Kong, SAR, China, from March 2015 to April 2015. His current research interests include antenna design, especially broadband antennas, circularly polarized antennas, electrically small antennas, and their applications. In 2014, he served as one of the TPC Co-Chairs for the 2014 IEEE International Workshop on Electromagnetics: Applications and Student Innovation Competition and in 2017, he served as one of the General Chairs for the IEEE International Conference on Computational Electromagnetics. He served as an Associate Editor for *IEICE Transactions on Communications*, from 2012 to 2016, and he was also an Associate Editor of IEEE TRANSACTIONS ON ANTENNAS AND PROPAGATION, from 2015 to 2022.

• • •